ft value of the $0^+ \to 0^+$ β^+ decay of ^{32}Ar: A measurement of isospin symmetry breaking in a superallowed decay

M. Bhattacharya,[1,2] D. Melconian,[2,3,*] A. Komives,[4,5] S. Triambak,[2] A. García,[2,5] E. G. Adelberger,[2] B. A. Brown,[6,7] M. W. Cooper,[8] T. Glasmacher,[6,7] V. Guimaraes,[9] P. F. Mantica,[7,10] A. M. Oros-Peusquens,[7,†] J. I. Prisciandaro,[7,10] M. Steiner,[7] H. E. Swanson,[2] S. L. Tabor,[8] and M. Wiedeking[8]

[1]*Brookhaven National Laboratory, P. O. Box 5000, Upton, New York 11973-5000, USA*
[2]*Physics Department, University of Washington, Seattle, Washington 98195, USA*
[3]*Department of Physics, Texas A&M University, College Station, Texas 77843-3366, USA*
[4]*Department of Physics and Astronomy, DePauw University, Greencastle, Indiana 46135, USA*
[5]*Department of Physics, University of Notre Dame, Notre Dame, Indiana 46556, USA*
[6]*Department of Physics and Astronomy, Michigan State University, East Lansing, Michigan 48824, USA*
[7]*National Superconducting Cyclotron Laboratory, Michigan State University, East Lansing, Michigan 48824, USA*
[8]*Department of Physics, Florida State University, Tallahassee, Florida 32306, USA*
[9]*Instituto de Fisica, University of São Paulo, C. P. 05389-970, São Paulo, Brazil*
[10]*Department of Chemistry, Michigan State University, East Lansing, Michigan 48824, USA*

(Received 3 April 2008; published 24 June 2008)

We determined the absolute branch of the $T = 2$ superallowed decay of ^{32}Ar by detecting the β^+-delayed protons and γ decays of the daughter state. We obtain $b^{\beta}_{\mathrm{SA}} = (22.71 \pm 0.16)\%$, which represents the first determination of a proton branch to better than 1%. Using this branch along with the previously determined ^{32}Ar half-life and energy release, we determined $ft = (1552 \pm 12)$ s for the superallowed decay. This ft value, together with the corrected $\mathcal{F}t$ value extracted from previously known $T = 1$ superallowed decays, yields a measurement of the isospin symmetry breaking correction in ^{32}Ar decay $\delta_C^{\mathrm{exp}} = (2.1 \pm 0.8)\%$. This can be compared to a theoretical calculation $\delta_C = (2.0 \pm 0.4)\%$. As by-products of this work, we determined the γ and proton branches for the decay of the lowest $T = 2$ state of ^{32}Cl, made a precise determination of the total proton branch and relative intensities of proton groups that leave ^{31}S in its first excited state and deduced an improved value for the ^{32}Cl mass.

DOI: 10.1103/PhysRevC.77.065503 PACS number(s): 23.50.+z, 23.40.−s, 23.20.Lv, 27.30.+t

I. INTRODUCTION

A. Motivation

Precise determinations of the ft values for $0^+ \to 0^+$ superallowed weak nuclear decays are a powerful tool to search for new physics. These data have been used [1,2] to test the unitarity of the Cabibbo-Kobayashi-Maskawa (CKM) mass-mixing matrix as well as to place limits on scalar and right-handed currents. However, before the measured ft values can be used for these purposes, they must be corrected for radiative processes and isospin-symmetry-breaking corrections. It is customary to define a corrected $\mathcal{F}t$ value:

$$\mathcal{F}t \equiv ft(1-\delta_C)(1+\delta_R) = \frac{K}{G_F^2|V_{ud}|^2|M_{fi}|^2\left(1+\Delta_R^V\right)}. \quad (1)$$

Here $K/(\hbar c)^6 \equiv 2\pi^3\hbar \ln 2/(m_e c^2)^5$, G_F is the Fermi coupling constant derived from muon decay, $|V_{ud}|$ is an element of the CKM matrix, and vector current conservation requires the Fermi matrix element to be $|M_{fi}|^2 = T(T+1) - T_Z(T_Z \mp 1)$, where T is the isospin of the multiplet and $T_Z \equiv \frac{1}{2}(Z-N)$. The remaining parameters are theoretical corrections that account for departures from strict isospin symmetry. Δ_R^V is the nucleus-*independent* radiative correction; δ_R is the nucleus-*dependent* radiative correction, which is the sum of a structure-*independent* (δ_R') and structure-*dependent* (δ_{NS}) components; and δ_C is the nucleus-*dependent* isospin-symmetry-breaking correction. These corrections are all of the order of a few percentages.

The standard model predicts identical $\mathcal{F}t$ values for all $J^\pi = 0^+, T = 1 \to J^\pi = 0^+, T = 1$ decays. It is gratifying that the $\mathcal{F}t$ values of the nine most precisely known $T = 1$ superallowed decays are constant to better than one part in 3×10^4 [1]; the mean $\mathcal{F}t$ value for these $T = 1$ superallowed transitions is [2]:

$$\overline{\mathcal{F}t}(T=1) = 3072.3(1.2)\mathrm{s}. \quad (2)$$

In this article we investigate the isospin-symmetry-breaking correction δ_C by studying the $T = 2$ superallowed β^+ decay of ^{32}Ar, which is expected [3] to have an unusually large correction as shown in Fig. 1. The isospin symmetry breaking corrections are customarily separated into a "configuration mixing" part, δ_C^{cm}, that accounts for the charge-dependent mixing with other 0^+ states, and a "radial overlap" part, δ_C^{ro}, that accounts for the fact that the mean-field for the "parent proton" and "daughter neutron" is modified by the isospin-non-conserving Coulomb interaction (see Refs. [6–9]). For the nine most precisely known $T = 1$ cases δ_C^{ro} is the

*dmelconian@physics.tamu.edu
†Present address: Institute of Medicine

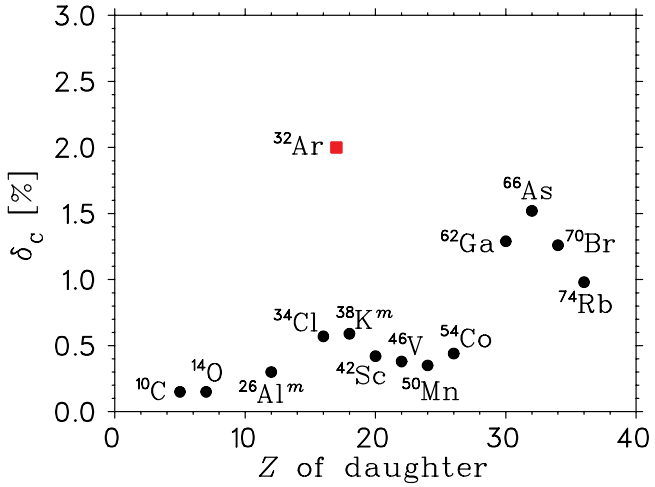

FIG. 1. (Color online) Predicted isospin-symmetry-breaking correction, δ_C, versus Z for a number of superallowed decays (from Ref. [6]) as well as our calculation for ^{32}Ar.

dominant part of the isospin-symmetry-breaking correction. It is therefore valuable to check the calculations in systems where these "radial overlap" corrections are inherently large. We studied ^{32}Ar because the radial overlap effect is enhanced near the proton drip line where the rms radius of the valence orbits changes most rapidly with Z. Similar effects are also present in the $T=1 \rightarrow T=1$ multiplets but are less significant because these states are more tightly bound. The predicted ^{32}Ar correction, $\delta_C = (2.0 \pm 0.4)\%$, can be decomposed into $\delta_C^{\rm cm} = 0.6\%$ and $\delta_C^{\rm ro} = 1.4\%$.

B. Experimental technique

We measured the absolute branching ratio for the ^{32}Ar superallowed β^+ decay by implanting ^{32}Ar ions in a silicon detector and counting their subsequent decays. Absolute β branches can be determined in implantation experiments using either of the following two techniques: (1) one can continuously count implanted parent ions along with the decay products and at the end of the experiment compute the ratio of the total number of decay products to the total number of implanted parent ions or (2) one can correlate each implantation with its corresponding decay, ensuring a high signal-to-background ratio because decay products are counted only after an ion of interest (which can be defined using stringent constraints) has arrived. In the case of ^{32}Ar with $t_{1/2} = 100.5(3)$ ms [10], the second technique would have limited the incoming rate to $\approx$2 ions/s because in this case one must wait a substantial period (>5 half-lives) before implanting another ion. We therefore used the first method and implanted ions at a rate of $\approx$20 s^{-1} to obtain the statistics necessary for a determination of the branch with better than 1% uncertainty. The problem of sacrificing statistics for a good signal-to-background ratio can in principle be avoided by using a segmented counter, but concerns [11] about the efficiencies of the intersegment sites led us to use unsegmented detectors.

II. EXPERIMENTAL SETUP

^{32}Ar ions were produced at the National Superconducting Cyclotron Laboratory (NSCL) by fragmenting a 100 MeV/u ^{36}Ar^{+12} beam on a 470 mg/cm^2 ^{9}Be target. The ^{32}Ar ions were separated from the other nuclides created in the process by passing the beam through the A1200 fragment separator. The two dipoles of the A1200 were set at 2.08112 and 1.89409 T-m, respectively. A 133-mg/cm^2-Al-equivalent plastic wedge inserted between the two dipoles gave additional fragment separation because the energy lost in the wedge depended on the nuclear charge as well as on the velocity of the ion. The ^{32}Ar beam left the A1200 with a momentum spread of $\Delta p/p \approx 1\%$. It then passed through the Reaction Product Mass Separator (RPMS) Wien filter, which transmitted particles only within a narrow velocity window, further purifying the 53.28 MeV/u ^{32}Ar beam.

Our detector array, shown in Fig. 2, consisted of a PIN silicon detector (D_1) and a stack of three fully depleted 450-mm^2-area, 500-μm-thick silicon surface barrier detectors (D_2, D_3, and D_4) surrounded by five large-volume high-purity Ge (HPGe) detectors (G_{1-5}). A 310-μm-thick aluminum foil inserted between D_1 and D_2 ensured that the incoming ^{32}Ar ions stopped in the middle of D_3 (the implantation detector). Signals from D_2, D_3, and D_4 were processed by Canberra 2001 preamplifiers that had low thresholds for detecting βs as well as the much larger signals from the incoming heavy ions. D_1 provided energy loss and time-of-flight information that was used for identifying incoming fragments. The energy loss in D_2 in conjunction with the energy deposited in D_3 gave an independent identification of the stopping ions that was used to determine the actual number of ions implanted in D_3. The implantation detector also served as our delayed proton counter. D_2 and D_4 were used to reject fast light charged particles and served also as β detectors. D_4 also helped us reject ^{32}Ar ions that did not stop in D_3. Our trigger consisted of any

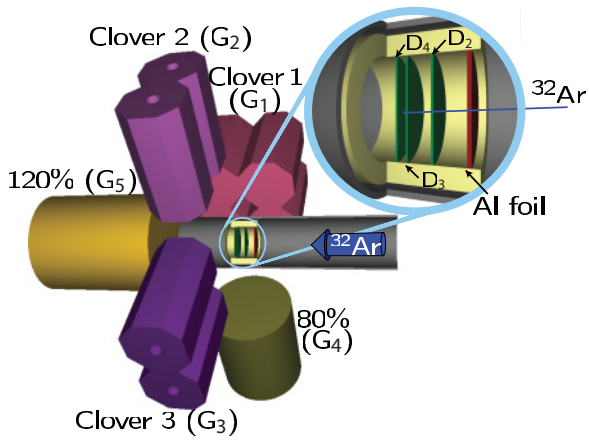

FIG. 2. (Color online) Schematic view of the experiment (to scale) with the Ge and Si detectors labeled. The ^{32}Ar ion beam first passes through the D_1 PIN diode (off scale to the right), then goes through the D_2 detector before stopping in the middle of D_3. Half of clovers 2 and 3 have been cut away to show the position of the particle detectors in the beam line; this cutaway view is magnified in the top-right balloon to clearly show the relative Si detector positions.

event in detectors D_2, D_3, or D_4 resulting in a β-detection efficiency of $(95 \pm 1)\%$ (see Sec. V A). Because the Si wafers came from the factory attached toward one face of the ≈8.3-mm-deep Al mounting rings, D_4 could be placed close to D_3(≈2.0 mm away), whereas D_2 was necessarily further away (≈8.3 mm). The array of HPGe detectors consisted of three 4-fold segmented "clover" detectors [12] (G_1, G_2, and G_3, each with efficiencies of ≈120%) and two monolithic crystals (G_4 and G_5, with efficiencies of 80 and 120%, respectively).

III. INCOMING ION EVENTS

A. Strategy

We separated events into *incoming ions* and *decays*. The former consisted of events in which D_1, D_2, and D_3 registered energies larger than ≈0.1 GeV, and no energy was deposited in D_4. *Decay* events left between 114 keV and 11.5 MeV in D_3 and/or between 55 keV and 5.5 MeV in either D_2 or D_4; in all cases, *decay* events were required to have not deposited any energy in D_1. *Incoming ions* were further separated into three categories. *Good* ions stopped in D_3 and were clearly identified as ^{32}Ar ions in both the E_1 vs. TOF_1 (energy and time-of-flight measured with D_1) and the E_3 vs. E_2 spectra. We created *buffer* regions in the particle identification spectra that included ions we could not guarantee were ^{32}Ar ions; we made sure that these regions were large enough so that no ^{32}Ar ion whose proton emissions could have been detected by D_3 could lie outside the union of the *good* and *buffer* regions. The ions in the *buffer* regions were labeled as *ambiguous*. *Contaminant* ions were all those not contained in either of the above two groups. To avoid contaminating our delayed proton and γ spectra by decay products of *ambiguous* ions, we rejected all *ambiguous* ions and imposed a 500-ms software dead time (about five ^{32}Ar half-lives) on counting either incoming ions or proton decays following the implantation of an *ambiguous* ion. If another *ambiguous* ion was detected within 500 ms of the previous *ambiguous* ion, the software dead time was reset to count for another 500 ms.

B. Ion identification

Incoming ions were identified with the help of the code LISE [13]. Figure 3 shows the E_1 versus TOF_1 spectrum; the area labeled "Region 3.1" contains mainly ^{32}Ar ions but is not clearly separated from contaminants. Region 3.2, which surrounds the main ^{32}Ar group in Region 3.1, mostly contains *ambiguous* ions. Figure 4 shows the E_3 versus E_2 spectrum of all events in Fig. 3. Figure 5 is similar to Fig. 4 but contains only events in Region 3.1 of Fig. 3. Region 5.1 of Fig. 5 contains the *good* ^{32}Ar ions; the remaining events are ^{32}Ar ions that either reacted before reaching D_3 or whose full energy was not detected in D_3.

Before we describe our criteria for separating *good* ions from *ambiguous* ions, we explain some peculiar features in our particle identification spectra.

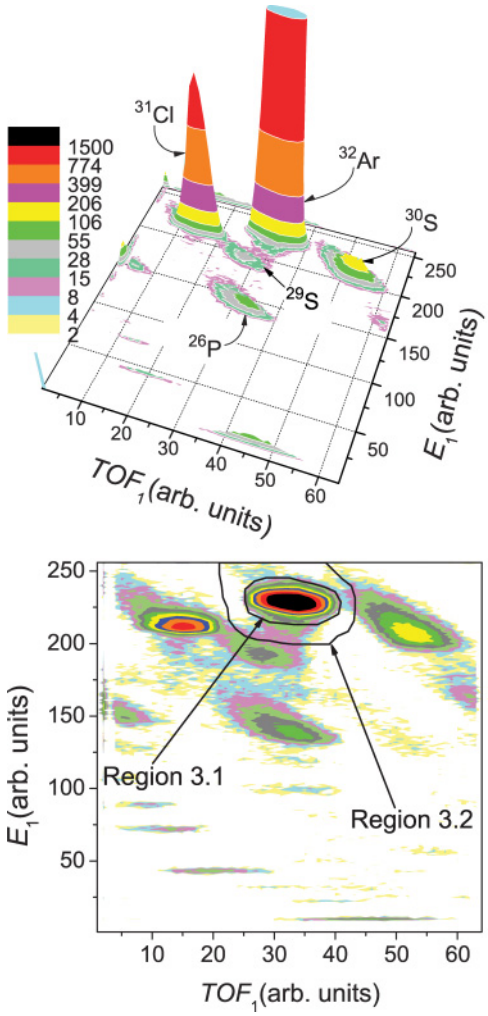

FIG. 3. (Color online) E_1 versus TOF_1 spectrum from a single run. (Top) Surface plot where the ^{32}Ar group has been truncated to show the other groups more clearly. (Bottom) Vertical projection showing Region 3.1, which contains the main ^{32}Ar group, and Region 3.2 that surrounds Region 3.1, which contains mostly ambiguous ions.

(i) *Saturation effects*. In Fig. 4 the horizontal line in the high E_3 region and vertical line in the high E_2 region are due to saturation of the preamplifier signals. To obtain the best possible energy resolution we used a single preamplifier on each detector; therefore the preamplifiers had to process an unusually wide range of energies.

(ii) *Events in Region 4.1*. Figure 6 shows the E_1 versus TOF_1 spectrum for events in Region 4.1, showing that these events originate in a high-energy tail in the beam profile. These ions left less energy in D_1 and D_2 but more in D_3 than the *good* ^{32}Ar ions, as one would expect from a high-energy tail. Other effects, such as channeling in D_1, could lead to the same features as seen in Fig. 4, but then E_1 would be independent of TOF_1 which is not what we observe (see Fig. 6).

(iii) *Vertical line descending from the main ^{32}Ar group in Fig. 5*. These events are the combined results of ^{32}Ar

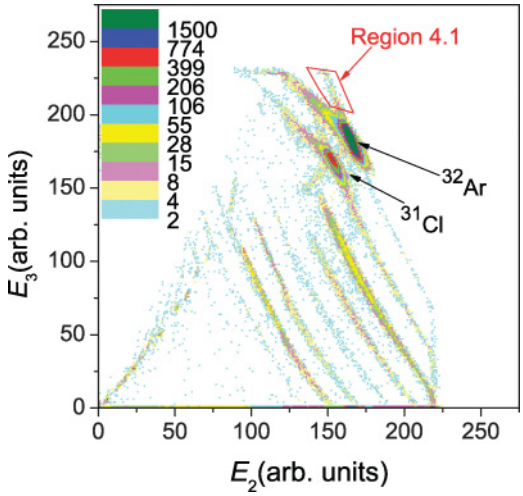

FIG. 4. (Color online) E_3 versus E_2 spectrum of events shown in Fig. 3. Region 4.1 was defined to show that the events in this region arise from a high-energy tail of the beam and to define Region 6.1 (see text and Fig. 6).

ions that landed near the edge of D_3 after scattering in D_2 and those that reacted before coming to rest. This was confirmed in our Monte Carlo calculations (which are described below).

(iv) 45° *line descending from main* ^{32}*Ar group in Fig.* 5. We are able to select this structure by requiring events to register as a heavy-ion event but to give signals below the threshold of the high-gain ADCs for D_2 and D_3. Figure 7 shows that this is an efficient vetoing strategy. These events apparently resulted from high-voltage breakdowns in the RPMS that occurred at about the same time as a heavy-ion was passing through. The breakdown produced intense x-ray bursts that loaded down our particle counters. Events in this 45° line are from ions that arrived before the detectors had fully recovered.

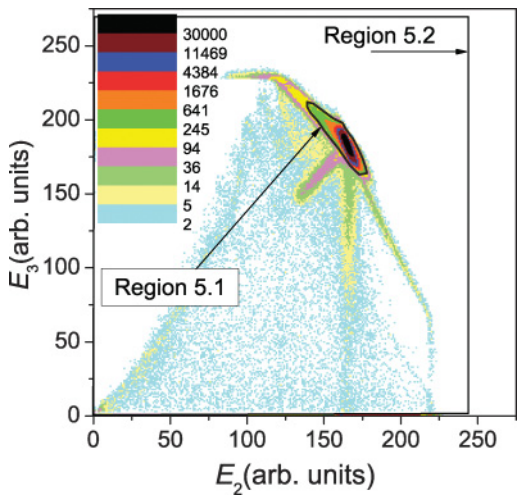

FIG. 5. (Color online) E_3 versus E_2 distribution of events in Region 3.1 in Fig. 3. Region 5.1 contains *good* ^{32}Ar ions and has 61 times more events than the surrounding Region 5.2 which contains *ambiguous* ions.

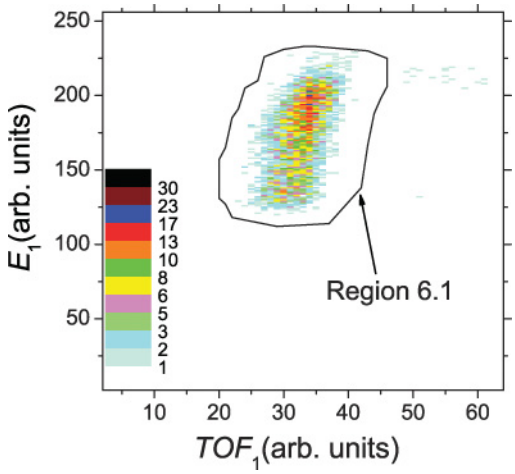

FIG. 6. (Color online) E_1 versus TOF_1 distribution of events in Region 4.1. The correlation between TOF_1 and E_1 shows that these events arise from a high-momentum tail of the implanted ion distribution.

C. Number of implanted ^{32}Ar ions

We used the following criteria to tag ^{32}Ar ions as *good* or *ambiguous*. *Good* ^{32}Ar ions had to appear in Regions 3.1 and 5.1, without depositing any energy in D_4. *Ambiguous* ions, however, had to appear in either

(i) Region 3.2 *and* either Region 5.1 *or* 5.2,
(ii) Region 3.1 *and* Region 5.2 (which excludes Region 5.1),
(iii) Regions 3.1 and 5.1 (much like a *good* ion) but also depositing energy in D_4,

or to fall under the categories of subsections 2 and 4 defined in the previous section (the high-momentum tail of the incoming beam and the "45° line"). Thus, all of the features described

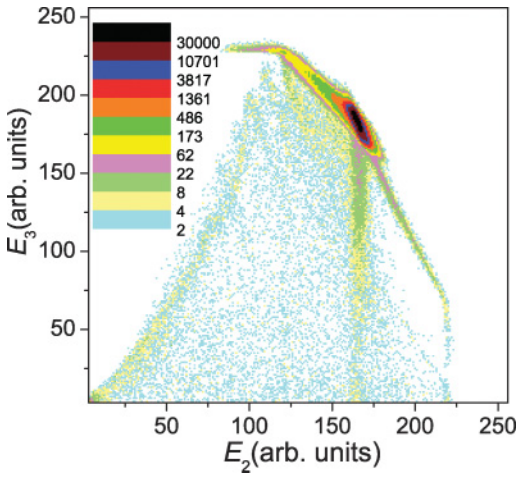

FIG. 7. (Color online) Same as Fig. 5, except that events corresponding to sparks in the RPMS (see text) have been rejected.

in Sec. III B are encompassed by our definition of *ambiguous* ions.

To check if the non-Gaussian features in the momentum distribution of the beam profile could have caused ^{32}Ar ions to appear in the *contaminant* regions of the E_1 vs. TOF_1 spectrum, we generated an E_3 vs. E_2 spectrum gated by *contaminant* ions. The resulting spectrum contained no events that corresponded to mass 32.

A total of $N_{\mathrm{Ar}} = 2\,241\,359$ *good* ^{32}Ar ions (not preceded by an *ambiguous* ion in 500 ms) were implanted, along with $N_{\mathrm{a}} = 158\,584$ *ambiguous* ions and $N_{\mathrm{c}} \approx 1.000 \times 10^6$ *contaminant* ions.

If any of the *ambiguous* events were ^{32}Ar ions, then at most $2^{-500/t_{1/2}} = (3.18 \pm 0.03)\%$ of their decays would occur after the 500-ms veto period had ended and would be indistinguishable from the decay products of *good* ^{32}Ar ions. We corrected for this effect by averaging the two extreme cases: that all *ambiguous* ions were ^{32}Ar ions and that *no ambiguous* ions were ^{32}Ar ions. We added this average to N_{Ar} with a 100% uncertainty to obtain:

$$N_{\mathrm{Ar}}^{\mathrm{uncorr}} = 2.244(3) \times 10^6, \tag{3}$$

for the number of incoming ^{32}Ar ions without corrections for fragmentation. We discuss the effect of fragmentation in subsection A1 and show it requires a $(0.2 \pm 0.2)\%$ correction. We consequently adopt

$$N_{\mathrm{Ar}} = 2.239(5) \times 10^6. \tag{4}$$

Because the gates defined by Regions 3.1 and 5.1 are so narrow (note the purity of ^{32}Ar in Fig. 5 compared to Fig. 4), the probability that a contaminant ion satisfied both gate conditions was negligible.

IV. β-DELAYED PROTON BRANCHES

Figure 8 shows the energy spectrum of *decay* events in D_3 for one of our 21 ^{32}Ar runs (approximately 3% of the total data set). The prominent peak at $E_p \approx 3500$ keV was produced by delayed protons following the superallowed decay of ^{32}Ar (see Fig. 9 for a simplified decay scheme). The proton lines have pronounced high-energy tails (cf. Fig. 10) from the summing with the energy deposited by the escaping positrons (i.e., $E_3 = E_p + E_\beta$). The structure below $E_3 \approx 1.2$ MeV is dominated by β decays that did not produce protons (such as ^{32}Ar decays to particle-bound states of ^{32}Cl, or implanted ^{31}Cl ions that decay mainly to the ^{31}S ground state). The spectrum is dominated by β-delayed proton decays to the ground and first excited states of ^{31}S (the p_0 and p_1 groups, respectively). We did not find any evidence for β-delayed proton decay to the third excited state of ^{31}S (p_3 branch), and only a weak branch for the Fermi transition followed by protons leaving ^{31}S in its second excited state (p_2 branch). The other peaks, most prominently at $E_3 = 2.3$ and 2.6 MeV in Fig. 8 and $E_p = 2.1$ and 2.4 MeV in Fig. 10, originate from Gamow-Teller transitions. These transitions are not relevant for isospin mixing of the isobaric analog state (IAS), but will be used to calculate the total feeding of the ^{31}S first excited state and are

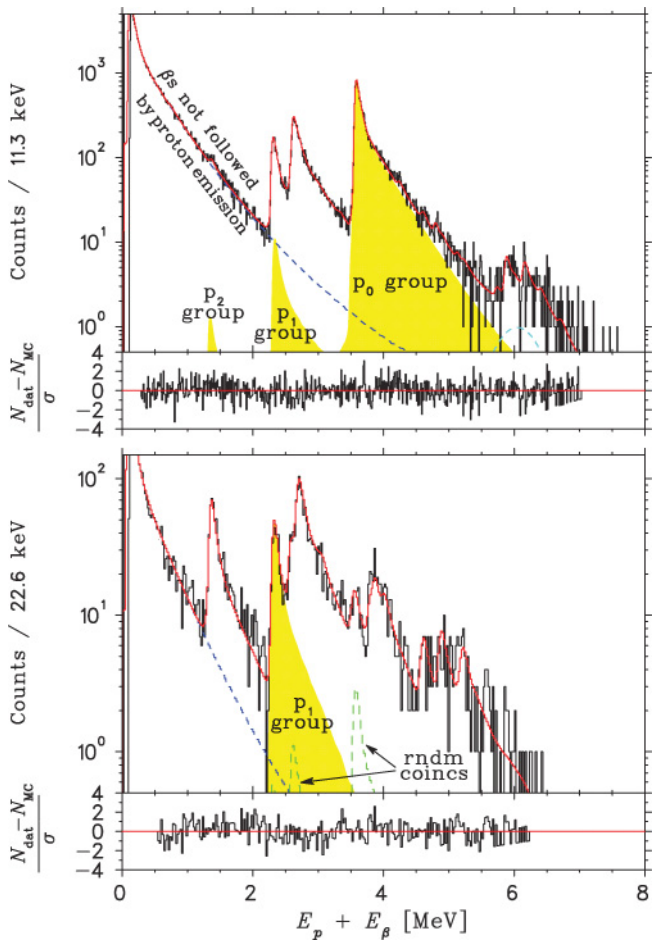

FIG. 8. (Color online) (Top panel) Singles delayed proton spectrum in D_3 for a typical run (histogram) along with the fit to the Monte Carlo simulation (solid line). The filled curves correspond to proton emission following the superallowed transition and the dashed lines are the backgrounds. (Bottom panel) Same as above but all runs added together and gated by $E_\gamma = 1249$ keV which selects the p_1 group at $E_p \approx 2.3$ MeV. In both cases, the ratio of the residuals to the standard deviation for each point is shown below the corresponding spectrum.

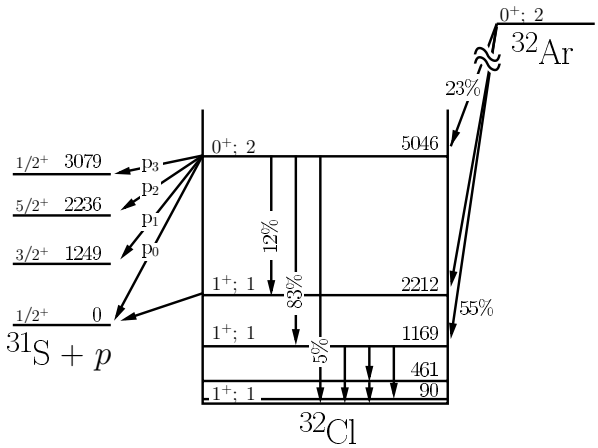

FIG. 9. Simplified ^{32}Ar decay scheme showing observed transitions that produce γ rays.

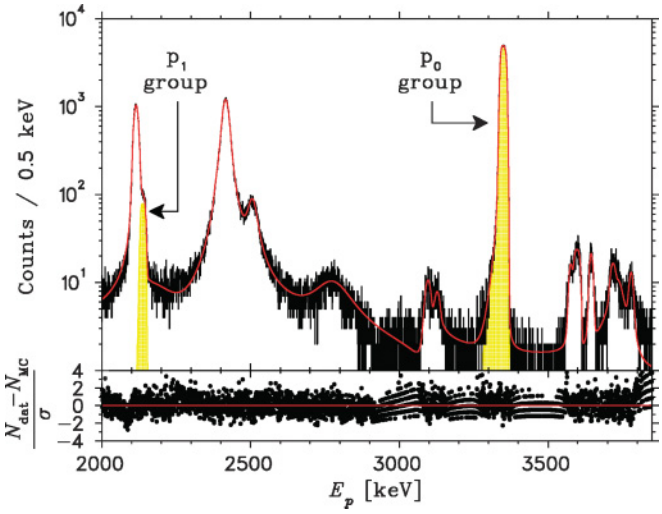

FIG. 10. (Color online) (Upper panel) ISOLDE data and R-matrix fit. (Lower panel) Ratio of residuals to standard deviation for each point. This spectrum was taken by implanting 60-keV ^{32}Ar ions into a 20 μg/cm^2 carbon foil and observing the β-delayed proton groups with cooled PIN diodes. The detection setup was immersed in a 3.5-T magnetic field that prevented the β^+s from reaching the detectors and summing with protons.

necessary to include in the R-matrix fit to account for their overlap with the superallowed peaks.

We determined the areas of the individual delayed proton peaks with the aid of previous data—a high-resolution (≈5-keV FWHM) proton spectrum obtained at ISOLDE [10,14] shown in Fig. 10, and branching ratios (relative to the superallowed group) of nine weakly populated states with $E_p > 4$ MeV as measured in Ref. [16].

The ISOLDE spectrum was fitted using an R-matrix formalism for overlapping, interfering daughter states [15] that parameterized the intrinsic delayed proton spectrum in terms of the transition matrix elements, energies and proton widths of 19 daughter states. The R-matrix spectra were separated into four noninterfering groups corresponding to proton emission leaving the ^{31}S in its ground and first three excited states for Fermi transitions and another four corresponding to Gamow-Teller transitions. These R-matrix intrinsic shapes were folded with a detector response function consisting of a Gaussian folded with two exponentials as described in Ref. [14] to fit the data in Fig. 10, yielding the relative intensities, energies, and intrinsic widths of the proton groups with energies up to 4 MeV.

We fitted the MSU data in Fig. 8 by feeding our R-matrix intrinsic shapes, extracted from the ISOLDE data, into a Monte Carlo simulation of the MSU experiment. The level structure above $E_p = 4$ MeV, which was not determined by the ISOLDE data, was varied to fit Fig. 8 giving the results in Table I. Including a broad (≈360-keV FWHM) Gaussian peak at 6.05 MeV significantly improved the local χ^2. This peak was not reported in the tables of Ref. [16] but could arguably be present in their spectrum. However, we see no evidence of this broad peak when gating the D_3 spectrum on a β event in either D_2 or D_4. Therefore, the peak is not produced in an ^{32}Ar β^+ decay, but we cannot exclude the possibility of EC decay or a background. The uncertainties we quote below will include whether we assume this peak are ^{32}Ar or not. The weak extra peaks in the lower panel of Fig. 8 at 2.6 and 3.6 MeV originate from random coincidences with the Ge detectors.

TABLE I. p_0 groups with $E_p > 4$ MeV.[a]

This work			Ref. [16]	
E_p (keV)	E_x (keV) (in ^{32}Cl)	I_p(%)[b]	E_p (keV)	I_p(%)[b]
3984(5)	5695(5)	1.1(1)	3994	1.2(9)
4340(5)	6063(5)	0.71(7)	4341	0.70(9)
4529(8)	6259(8)	0.54(5)	4521	0.52(4)
4997(10)	6742(10)	0.10(2)	4975	0.06(2)
5567(5)	7330(5)	0.76(8)	5552	0.57(4)
5699(10)	7467(10)	0.18(8)	5675	0.05(3)
5833(5)	7605(5)	0.54(5)	5817	0.44(4)
6097(10)	7878(10)	0.11(2)	6060	0.09(2)
6396(10)	8186(10)	0.06(2)	6347	0.06(2)

[a]From the spectrum in the top panel of Fig. 8; p_1 groups are shown in Table II.
[b]Relative to the superallowed p_0 group.

We accounted for detector responses and for scattering by using GEANT [17] to track the decay products (protons, βs, and their associated annihilation radiation). These simulated spectra were then fitted with the following free parameters—the gain of the energy calibration, the Gaussian noise of the detectors, an overall normalization, and two parameters describing the β background (discussed below). The data were divided into 49 blocks of approximately equal numbers of implanted ions and then fitted separately. This separation was made because the extremely sharp rise of the p_0 peak made the results very sensitive to small changes in the gain of D_3 and, as shown in the top plot of Fig. 11, the level of background/contamination changed as the run progressed.

The largest background in the proton singles spectrum of Fig. 8 came from βs that were not followed by delayed protons. We simulated the shape and magnitude of this background using the decay scheme outlined in Fig. 9; we expect two of such β events per incoming ^{32}Ar, with end-point energies ranging from 1.4 to 12.2 MeV. The dashed curve in Fig. 8 shows the combined simulated β energy losses from ^{32}Ar, ^{31,32}Cl, and ^{31}S decays. Figure 11 shows that this background level changed somewhat as the run progressed, indicating earlier runs had a significantly worse ^{31}Cl contamination level than later ones.

A. Total proton branch in ^{32}Ar decay

The proton branching ratios were found by fitting each of the 49 blocks of β-delayed proton spectra individually and then averaging the results. The number of ions was simultaneously broken up, and the corrections described in Sec. III C were applied in each instance. Summing up the contributions from all R-matrix levels associated with ^{32}Ar decay and dividing by N_{Ar} gave the results shown in the bottom plot of Fig. 11. The fit to the average of all 49 blocks had a χ^2 per 48 degrees of

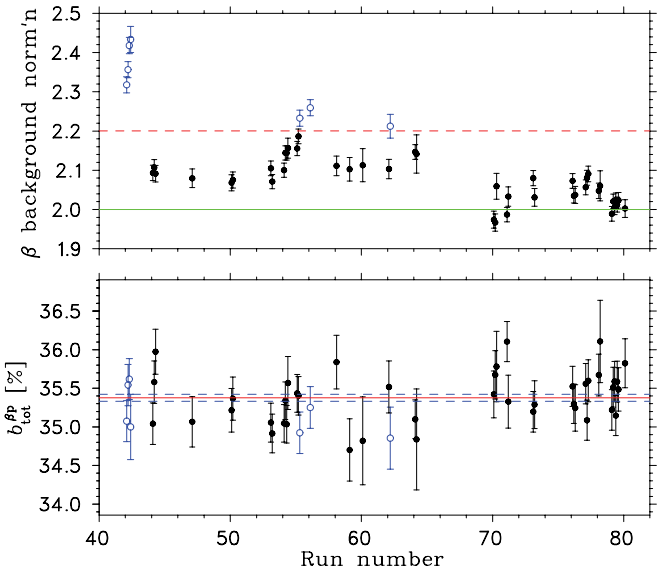

FIG. 11. (Color online) Total proton branches (bottom) and background levels (top) deduced from fitting all of the D_3 spectra to MC simulations. A sample of one of these fits is given in the top panel of Fig. 8, where we show the result for run 78. The open circles are runs where the contaminant level of ^{32}Cl resulted in a background level that was more than 10% above what we would expect based on the decay chain of ^{32}Ar. For this reason, these runs (above the dashed line in the top plot) were excluded from the fit to $b_{\rm tot}^{\beta p}$ shown in the bottom plot.

freedom of 1.11, resulting in an acceptable confidence level of 29%. Note that the extracted $b_{\rm tot}^{\beta p}$ is not significantly correlated with the differing background levels. Indeed, if we sacrifice 16% of the data by fitting only runs where the background was less than 2.2 (i.e., the filled points in Fig. 11), the reduced χ^2 remains the same and $b_{\rm tot}^{\beta p}$ increases by less than half the statistical error. However, to be conservative, we include in our systematic uncertainty the change in $b_{\rm tot}^{\beta p}$ when this background is fixed to the expected 2βs per ^{32}Ar ion compared to when it was a free parameter. Our final result is

$$b_{\rm tot}^{\beta p} = \frac{N_p^{\rm tot}}{N_{\rm Ar}} = (35.58 \pm 0.05 \pm 0.21)\%, \tag{5}$$

where the first uncertainty is statistical and the second is systematic.

This value as well as that in Eq. (7) differ from previous results quoted in Ref. [16]. The authors of Ref. [16] did not count the absolute number of incoming ^{32}Ar ions but deduced the branches by making certain assumptions. In particular, they deduced the total proton branch in two independent ways:

(i) They obtained $b_{\rm tot}^{\beta p} = (40 \pm 4)\%$ (in rough agreement with our result) by inferring the total number of implanted ^{32}Ar ions from the total number of βs detected. This method is problematic because it is hard to know what fraction of the β emission is from contaminants.

(ii) They obtained $b_{\rm tot}^{\beta p} = (43 \pm 3)\%$ by assuming that the superallowed transition is followed only by proton emission, and by assuming that the entire Fermi strength, $B(F) = 4$, resides in the superallowed transition. Nevertheless, we will show in Sec. V that the $T = 2$ state has an $\approx 10\%\gamma$ branch. In addition the end-point energy is now known to be lower than the value used in Ref. [16] by about 21 keV; using the correct end-point energy would decrease their deduced branch by $\approx 2\%$. Finally, isospin symmetry breaking effects are expected to reduce $B(F)$ by $\approx 2\%$. When these corrections are included the number quoted above translates to $b_{\rm tot}^{\beta p} = (37 \pm 3)\%$, in agreement with our value.

B. Delayed proton branches following the superallowed decay

The proton branching ratio of the ^{32}Cl isobaric analog state (IAS) to the ^{31}S ground state (p_0 group), deduced from $b_{\rm tot}^{\beta p}$ using the relative intensities from the ISOLDE data, is

$$b_{p_0}^{\beta p} = (20.50 \pm 0.03 \pm 0.12)\%. \tag{6}$$

The peak at 2.3 MeV, clearly visible in the bottom of Fig. 8, corresponds to proton emission from the IAS to the first excited level in ^{31}S (the p_1 group). This peak appears in the ISOLDE spectrum (Fig. 10) as a partially resolved shoulder on the right of the structure at 2.1 MeV. We obtained $N_{p_1}/N_p 0 = (1.25 \pm 0.10)\%$ from the NSCL data and $N_{p_1}/N_{p_0} = (1.29 \pm 0.04)\%$ from the ISOLDE data. We adopted the weighted average[1] $N_{p_1}/N_p 0 = (1.28 \pm 0.04)\%$.

We saw no evidence for p_2 and p_3 decays to ^{31}S states at $E_x = 2235.6$ keV and $E_x = 3079$ keV, respectively. We used the ISOLDE spectrum to obtain: $N_{p_2}/N_{p0} = (0.12 \pm 0.04)\%$ and $N_{p3}/N_{p0} = (0.07 \pm 0.07)\%$. These numbers are consistent with the upper limits obtained from this work.

We find a total proton branch for the superallowed transition of

$$b_{\rm SA}^{\beta p} = b_{p0}^{\beta p}\left(1 + \sum_{i=1,3} \frac{N_{p_i}}{N_{p0}}\right) = (20.79 \pm 0.07 \pm 0.12)\%. \tag{7}$$

Additional potential systematic effects are discussed in Sec. A2 and are shown to be negligible compared to the total uncertainty. This the first time a delayed proton branch has been measured with a precision better than 1%.

C. Delayed proton transitions feeding the ^{31}S first excited state

In addition to the p_1 superallowed group described above, we found several proton groups corresponding to p_1 decays following Gamow-Teller transitions. The lower panel of Fig. 8 shows the E_3 spectrum of events in coincidence with the 1249-keV γ ray in any of the five Ge detectors. Once we

[1] Although this Fermi peak does not interfere with its neighboring Gamow-Teller peaks, its intensity extracted from the ISOLDE spectrum varied by $\approx 20\%$ depending on the assumed sign of the GT-GT interference between the state at $E_p = 2.1$ MeV and tails from other resonances, mainly from the wide resonance at $E_p = 2.4$ MeV. We removed this ambiguity by requiring the R-matrix parameters to fit simultaneously the spectra in Fig. 10 and both panels of Fig. 8.

TABLE II. Proton groups in coincidence with a 1249-keV γ ray from the coincidence spectrum in Fig. 8.

This work[a]			Ref. [16]	
E_p (keV)	E_x (keV) (in ^{32}Cl)	I_p(%)[b]	E_p (keV)	I_p(%)[b]
912(5)	3772(5)	0.07(4)	–	–
1218(5)	4087(5)	1.90(22)	1214(10)	1.8(2)
2145(5)	5046(5)	1.28(4)[c]	–	–
2394(5)	5302(5)	0.56(11)	–	–
2515(5)	5427(5)	2.93(11)	–	–
2870(5)	5794(5)	3(1)[d]	–	–
3581(5)	6528(5)	0.24(4)	3592(10)	0.83(9)
3649(5)	6599(5)	0.32(3)	3643(10)	0.39(9)
3785(5)	6738(5)	0.52(5)	–	–
4529(5)	7507(5)	<0.03[e]	4521(10)	0.52(4)
4630(5)	7611(5)	0.16(5)	4621(10)	0.17(4)
4869(5)	7857(5)	0.26(3)	4858(10)	0.26(4)

[a]From the spectrum in the bottom panel of Fig. 8, unless otherwise stated.

[b]Relative to superallowed proton group leaving ^{31}S in its ground state.

[c]This value comes mainly from the ISOLDE data, as discussed in Sec. IV B.

[d]This is a very broad peak, and therefore it is difficult to accurately quote its intensity.

[e]We observe much less strength at this proton energy in coincidence with a 1249-keV γ ray compared to Ref. [16], but our intensities agree in the singles spectrum.

identified the groups, we used the ISOLDE spectrum to obtain their relative intensities. This allowed us to infer the relative intensities of these groups without depending on the γ-ray efficiency. Consequently, to optimize statistics, the full data were used without the cuts needed to reject *ambiguous* ions. Table II lists the intensities of these proton groups relative to the intensity of the superallowed proton group populating the ^{31}S ground state. The intensities are only approximate and were obtained as areas under the R-matrix fits within a region corresponding to four times the width of the state.

V. β-DELAYED γ BRANCHES

Figure 12 shows the summed γ-ray spectrum from the five Ge detectors in coincidence with a *decay* event in D_2, D_3, or D_4. To optimize statistics we did not impose the *ambiguous* ion electronic dead time. Nevertheless, all of the visible peaks correspond to ^{32}Ar or ^{32}Cl decays that demonstrates that removing this condition did not introduce significant contaminations to the data.

A. β-detection efficiency

The trigger for our experiment was given by events that left more than 55 keV in D_2 or D_4, or more than 114 keV in D_3. Consequently, our γ-ray detection efficiency depended on the β detection efficiency. The probability of detecting a β particle in any of the above silicon detectors was determined

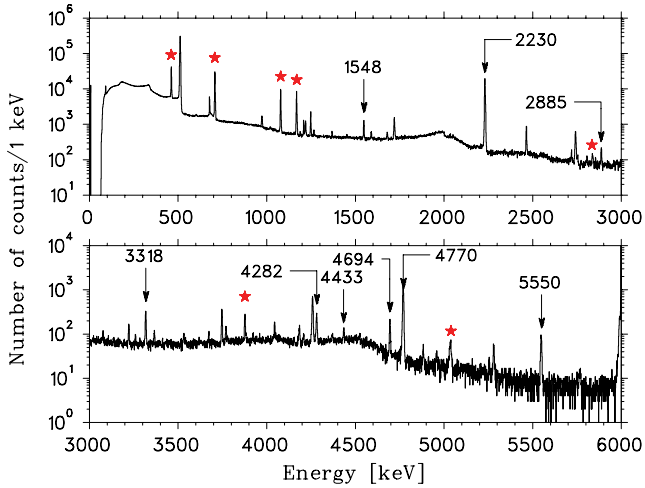

FIG. 12. (Color online) Spectrum of γ rays in coincidence with a β signal in D_2, D_3, or D_4. Lines from ^{32}Ar decay are marked with a "$*$". The remaining labeled lines are from ^{32}Cl decay. For all strong lines the corresponding sum peaks (with energy of 511 keV plus the photon energy) were clearly visible.

with a PENELOPE [18] simulation. We use PENELOPE in this case rather than GEANT because the former provides a better description of low-energy βs [19]; GEANT was used elsewhere when the analysis involved protons and heavy ions, which are not available in PENELOPE. Using the measured energy thresholds and assuming a ± 10 keV uncertainty in their values, the PENELOPE simulation indicates $\epsilon_\beta = 0.95(1)$. As we show below, our method for determining the γ-ray efficiencies does not depend significantly on ϵ_β which we present only for completeness.

B. HPGe detector γ-ray efficiencies

As Fig. 9 shows, $1 - b_{\rm tot}^{\beta p} = 64.5\%$ of the ^{32}Ar β decays are not followed by proton emission but rather feed the ground state of ^{32}Cl which itself is unstable β^+ decaying with a half-life of 0.3 s. The ^{32}Cl and ^{32}Ar decays have γ lines in the same energy range, so the known intensities of the ^{32}Cl lines [20] provide an in situ calibration of the HPGe detection efficiencies. The detection efficiency, ϵ_γ, of ^{32}Cl γ rays with energy E_γ registered in the $i^{\rm th}$ Ge detector is given by

$$N_{\rm Ar}\,\epsilon_\gamma^{(i)}(E_\gamma)\epsilon_\beta = \frac{\tilde{N}_\gamma^{(i)}}{\left(1 - b_{\rm tot}^{\beta p}\right) b^{\beta\gamma}(^{32}{\rm Cl})}, \qquad (8)$$

where $\tilde{N}_\gamma^{(i)}$ is the photopeak area corrected for summing effects and $b^{\beta\gamma}(^{32}{\rm Cl})$ is the known ^{32}Cl γ branch. The factor ϵ_β is the β detection efficiency described in the previous section. We show in Eq. (9) below that the factor on the left side of Eq. (8), rather than $\epsilon_\gamma^{(i)}$ alone, is needed to compute the γ branches following ^{32}Ar superallowed decay. This minimizes systematic uncertainties from the geometrical size and distribution of the source, as well as uncertainties from ^{32}Ar ions that could have escaped detection (i.e., ions that land outside the active area in D_3 but whose γs and βs could have been detected). The γ-ray efficiencies depend on the β thresholds

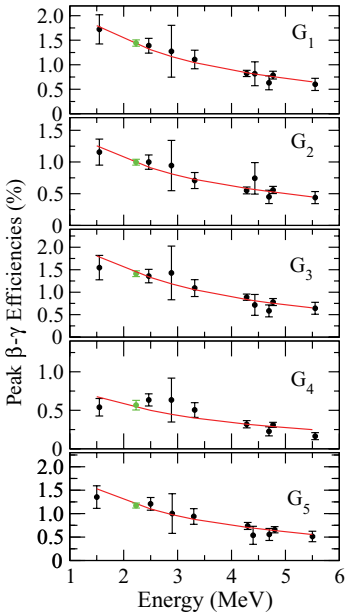

FIG. 13. (Color online) The absolute $\epsilon_\gamma \epsilon_\beta$ from ^{32}Cl decays (points) and the normalized PENELOPE curves for each detector (line). The point at 2.2 MeV was not used in normalizing the curves as explained in the text.

due to the different end points. However, our simulations indicate that this contribution to the total uncertainty of the γ branch is negligible.

Figure 13 shows the calculated efficiencies from the known ^{32}Cl lines along with PENELOPE calculations that describe the detectors' responses. These simulations accounted for matter outside the detectors that could attenuate or scatter γs and included the radial and depth distribution of the ^{32}Ar ions described in subsection A2. The 2230-keV peak from ^{32}Cl appears near a line at 2236 keV that is fed by decays of both ^{31}Cl and ^{32}Ar. Figure 13 shows the efficiency calculated at this energy even though the 2230-keV line was not used in fitting the efficiency curve because it was not clearly resolved in all of the detectors.

The measured ^{32}Cl points were fitted to the PENELOPE calculations with only the normalization free to vary. Once determined, the same normalization was applied to simulations at energies corresponding to the ^{32}Ar lines. Corrections for γ summing are dominated by summing with 511-keV annihilation radiation; however, both ^{32}Ar and ^{32}Cl undergo β^+ decay so this summing does not affect the ratios of peak areas. The summing with cascade γ rays, however, depends on the multiplicity and correlations of γ rays. We used the PENELOPE calculation to estimate these effects and calculate $\tilde{N}\gamma^{(i)}$ from the fitted photopeak areas. As an example of the magnitude of the summing corrections, $\tilde{N}\gamma^{(2)}$ for the 2230-keV γ ray from ^{32}Cl (which is always part of a cascade) is ≈5% larger than the measured number of counts. In the less efficient 80% detector, the summing correction is only ≈2%.

C. γ decays of the ^{32}Cl IAS

The lowest $T = 2$ state in ^{32}Cl decays predominantly by emitting protons. However, the proton decay of this state violates isospin symmetry, and the total width of this state is only ≈20 eV [10,14]. As a result, γ decays of this state cannot be neglected. Based on the decays of the isobaric analog states in ^{32}P and ^{32}S we expect γ decays to three 1^+ levels (see Fig. 9).

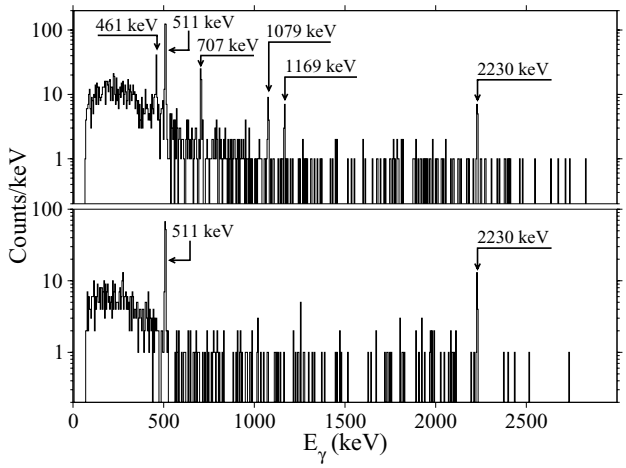

FIG. 14. (Top panel) Spectrum of γ rays in coincidence with a 3878-keV γ. All of the peaks except for the ones at 2230 and 511 keV correspond to the expected γ cascades following the 3878-keV γ ray. (Bottom panel) Same as above, but with the coincidence gate shifted down by 8 keV. This shows that the 2230-keV γ comes mainly from coincidences with the Compton continuum of the 4770-keV γ ray in ^{32}S.

The absolute γ-ray branches were computed as:

$$b^{\beta\gamma} = \frac{\sum_{i=1}^{5} \tilde{N}_\gamma^{(i)}}{N_{\mathrm{Ar}} \sum_{i=1}^{5} \epsilon_\gamma^{(i)} \epsilon_\beta}, \tag{9}$$

where the sum runs over all five Ge detectors.

The denominator on the right side of Eq. (9) comes from calibrations using lines from ^{32}Cl decay; this procedure makes the calculation of the branches rather independent of the distribution of parent ions and summing with 511-keV γs. The β-γ coincidence spectrum shown in Fig. 12 exhibits a peak at $E_\gamma = 3877.5(3)$ keV that is a candidate for the analog of the ^{32}P 5072 keV → 1149 keV transition. Figure 14 shows the spectrum of γ rays in coincidence with a 3878-keV γ ray in the β-γ coincidence spectrum (Fig. 12). The spectrum clearly shows the γ rays expected from de-excitation of the 1168.5(2)-keV state. This leads us to conclude that the decays originate in a state at $E_x = 5046.3(4)$ keV, after correcting for the nuclear recoil (see Sec. VI C4 for implications on the mass of ^{32}Cl). We have thus identified the isobaric analog of the ^{32}P 5072 keV → 1149 keV transition and we find its branch to be $b_{\mathrm{SA}}^{\beta\gamma}(E_\gamma = 3878\,\mathrm{keV}) = (1.58 \pm 0.08)\%$.

The ^{32}P $T = 2$ state also decays directly to the ground state, implying there should be a 5046-keV γ transition in ^{32}Cl. Unfortunately, the first escape peak of the 5550-keV γ ray from ^{32}Cl appears as a strong peak in the region of interest in the spectrum. Figure 15 shows data from G_5 (the 120% HPGe detector) and the corresponding fit. The 5046-keV peak was fitted with a fixed centroid, width and line shape,

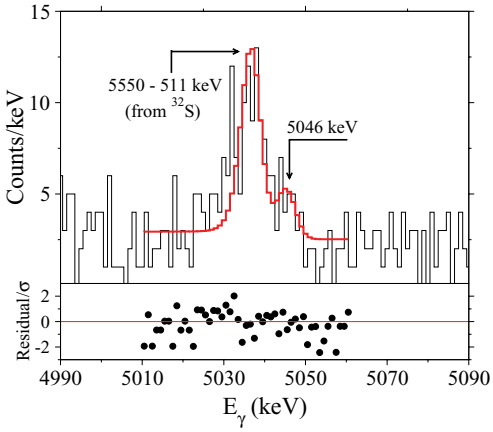

FIG. 15. (Color online) The region of interest where the γ ray corresponding to the decay from the $T = 2$ state to the ground state should appear at $E_\gamma = 5046$ keV. The main 5038-keV peak is the first escape from the 5550-keV γ ray from ^{32}Cl.

allowing only the background and area parameters to vary to obtain the photopeak yields from each detector. We obtain $b_{\mathrm{SA}}^{\beta\gamma}(E_\gamma = 5046\,\mathrm{keV}) = (0.098 \pm 0.021)\%$.

The analog of the 5072 keV $\rightarrow$ 2230 keV γ transition in ^{32}P is observed at $E_\gamma = 2836(1)$ keV, close to another peak at 2839 keV. As shown in Fig. 16, the identification was done by observing the corresponding coincident proton spectra. The energy of the proton group implies that it is emitted from a state[2] at 2212(5) keV which, when added to 2836(1) keV, yields $E_x = 5048(5)$ keV, consistent with the energy of the $T = 2$ state in ^{32}Cl. We obtain

[2]We used the Q_{p} value from Eq. (18) in Sec. VI C4.

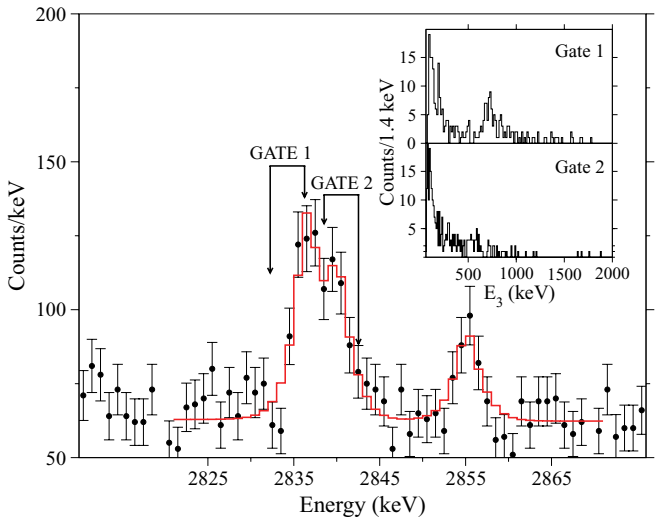

FIG. 16. (Color online) The 2836- and 2839-keV γ-ray doublet. The insets show the coincidence proton spectrum with GATE1 (which has a peak corresponding to 610-keV protons) and GATE2, respectively. This shows that the 2836-keV component is followed by proton emission, whereas the 2839-keV γ is not.

TABLE III. Absolute $\beta\gamma$ branches for ^{32}Ar β decays to the lowest $T = 2$ level of ^{32}Cl followed by γ emission.

E_γ (keV)	Absolute $\beta\gamma$ branch $b_{\mathrm{SA}}^{\beta\gamma}(\%)$
3878	1.58(8)
2838	0.24(3)
5046	0.10(2)

$b_{\mathrm{SA}}^{\beta\gamma}(E_\gamma = 2838\,\mathrm{keV}) = (0.24 \pm 0.03)\%$. This is significantly smaller than the $(0.39 \pm 0.07)\%$ intensity of 607-keV protons observed in singles by Bjornstad *et al.* [16], which correspond roughly to the same excitation energy. This can be explained by direct β feeding of the 2212-keV level in addition to γ feeding from the $T = 2$ state. The singles data from the NSCL experiment shows a small peak at $\approx$610 keV, but it is difficult to extract its area accurately because it sits on top of the intense β tails from decays that are not followed by particle emission. Our ISOLDE data yields $(0.385 \pm 0.008)\%$ for the intensity of this proton group, in agreement with Ref. [16].

The absolute intensities of the three γ decays of the $T = 2$ state are listed in Table III. We find the total β-delayed γ branch for the superallowed transition to be

$$b_{\mathrm{SA}}^{\beta\gamma} = (1.92 \pm 0.08 \pm 0.04)\%. \quad (10)$$

The sources contributing to the uncertainty are summarized in Table IV and discussed in subsection A3.

TABLE IV. Uncertainties contributing to the absolute superallowed branch in ^{32}Ar decay.

Component	$\Delta b_{\mathrm{SA}}^{\beta}/b_{\mathrm{SA}}^{\beta}[\%]$
Proton branch	
Implanted ^{32}Ar ions	$\pm$0.23
Number of p_0 protons	$\pm$0.53
Ratio of p_1/p_0 protons	$\pm$0.04
Ratio of p_2/p_0 protons	$\pm$0.04
Ratio of p_3/p_0 protons	$\pm$0.07
Proton decays near detector surface	$<$0.01
Sub-total	$\pm$0.58
γ branch	
Statistics in IAS decay peaks	$\pm$0.34
Statistics in ^{32}Cl decay peaks	$\pm$0.12
^{32}Cl branching ratios (from Ref. [20])	$\pm$0.11
Ge detector efficiency	$\pm$0.09
Sub-total	$\pm$0.39
Total	$\pm$0.70

VI. CONCLUSIONS

A. ft value of the superallowed decay

Adding the proton and γ branches, we obtain

$$b^{\beta}_{\mathrm{SA}} = \left(b^{\beta\gamma}_{\mathrm{SA}} + b^{\beta\mathrm{p}}_{\mathrm{SA}}\right) = (22.71 \pm 0.11 \pm 0.11)\%, \quad (11)$$

where $b^{\beta\gamma}_{\mathrm{SA}}$ and $b^{\beta p}_{\mathrm{SA}}$ are given by Eq. (10) and Eq. (7), respectively. Table IV summarizes the error budget for this superallowed decay branch.

A recent determination of the ^{32}Ar mass [21], along with our determination of the β-delayed proton energy [10] and the known masses of ^{31}S and the proton, implies

$$Q_{\mathrm{EC}} = 6.0913(25)\,\mathrm{MeV}, \quad (12)$$

which in turn yields a statistical phase-space factor [22]

$$f = 3506(8). \quad (13)$$

Using the ^{32}Ar half-life from an ISOLDE measurement [10],

$$t_{1/2} = 100.5(3)\,\mathrm{ms}, \quad (14)$$

we find that the superallowed decay has

$$ft(^{32}\mathrm{Ar}) = 1552(12)\,\mathrm{s}. \quad (15)$$

B. Experimental value for δ_C

We can now use our ft value from Eq. (15) in combination with Eq. (1) to obtain:

$$\delta_C^{\mathrm{exp}} = 1 - \frac{\overline{\mathcal{F}t}(T=1)}{2(1+\delta_R)\,ft(^{32}\mathrm{Ar})} = (2.1 \pm 0.8)\%, \quad (16)$$

where the factor of 2 corresponds to the ratio of squared matrix elements for $T = 2$ and $T = 1$ decays and we used $\delta_R = (1.145 \pm 0.041)\%$ [22]. This is in agreement with the prediction $\delta_C = (2.0 \pm 0.4)\%$.

A more stringent test of the prediction requires an experiment with higher accuracy as well as a more careful assessment of the theoretical uncertainty in δ_C. The predicted configuration mixing correction δ_C^{cm} arises mainly from mixing of the ^{32}Cl $T = 2$ state with a $T = 1$ state 0.26 MeV lower in energy. A more meaningful comparison to the theory can be made if the radial-overlap and configuration-mixing contributions to δ_C could be separated experimentally. This can be done using the β-ν correlation to determine where the rest of the Fermi strength lies. This information should come from a full analysis of the ISOLDE data [10].

Using the calculated value for δ_C, we obtain:

$$\mathcal{F}t = 1538(14)\,\mathrm{s}. \quad (17)$$

C. Spectroscopic information

1. Total proton branch

We obtained $b^{\beta p}_{\mathrm{tot}} = (35.58 \pm 0.22)\%$ for the total of all proton branches following ^{32}Ar decay.

TABLE V. γ branches of the lowest $T = 2$ states in the $A = 32$ multiplet. The ^{32}Cl results were extracted from this work; ^{32}S and ^{32}P branches from other work.

E_γ (MeV)	Relative γ branch (%)		
	^{32}Cl	^{32}S [23]	^{32}P [24]
3.9	83(4)	84.3(9)	85.7(8)
2.8	12(2)	7.4(7)	9.4(5)
5.1	5(1)	6.3(7)	4.7(6)

2. Width and branches for γ decays of $T = 2$ state

Table V compares the γ-ray branches of analogous decays of the lowest $T = 2$ states in the $A = 32$ multiplet. There is rough agreement with isospin conservation, which predicts that the branches should be independent of T_Z.

We combine our value for the $\beta\gamma$ branch of the $T = 2$ state (which we obtained as the ratio of $b^{\beta\gamma}_{\mathrm{SA}}/b^{\beta}_{\mathrm{SA}}$) and the total width $\Gamma = 20(5)$ eV from the ISOLDE data [10] to obtain $\Gamma_\gamma = 1.7(4)$ eV. The shell-model prediction using the USD interaction [25] yields $\Gamma_\gamma \approx 1.1(1)$ eV.

3. β-delayed proton emission to first excited state of ^{31}S

Table II presents the intensities of the proton groups corresponding to decays leaving ^{31}S in its first excited state (p_1 groups) relative to the intensity of the superallowed p_0 group. We found several new groups corresponding to p_1 decays.

4. Mass of the ^{32}Cl ground state

The superallowed proton energy and the γ energy following de-excitation from the IAS yield a more precise determination of Q_p, the proton separation energy of the ^{32}Cl ground state. The ISOLDE data [10] show that the total kinetic energy of the daughter p and ^{31}S in the superallowed decay is $E^{\mathrm{cm}} = 3465.0(4)$ keV. Combining this with $E_x(T=2) = 5046.3(4)$ keV (from Sec. V C) gives

$$Q_p = E_x(T=2) - E^{\mathrm{cm}} = 1581.3(6)\,\mathrm{keV}. \quad (18)$$

This result, along with the mass excesses of hydrogen and ^{31}S [26], yields a ^{32}Cl mass excess of

$$\Delta M(^{32}\mathrm{Cl}) = \Delta M(^{1}\mathrm{H}) + \Delta M(^{31}\mathrm{S}) - Q_p = -13337.0 \pm 1.6\,\mathrm{keV} \quad (19)$$

which is more precise than the previously accepted value of -13329.8 ± 6.6 keV [26].

ACKNOWLEDGMENTS

We thank Ian Towner for calculating the nuclear-dependent radiative correction and the phase-space factor, Dick Seymour for computing support and Maria J. G. Borge for comments that

improved the clarity of the text. The University of Washington researchers were supported by the DOE under grant DE-FG02-97ER41020. The Notre Dame, MSU, and FSU researchers were supported by the NSF under grants PHY-9901133, PHY-9528844, PHY-0244453, and PHY-9970991.

APPENDIX: SYSTEMATIC UNCERTAINTIES IN THE SUPERALLOWED BRANCHING RATIO

D. Number of implanted ^{32}Ar ions

1. Nuclear fragmentation

If a ^{32}Ar ion fragmented before coming to rest in D_3, it could be misidentified as a *good* ^{32}Ar ion. Two independent parametrizations of the total reaction cross sections by Shen *et al.* [27] and Tarasov *et al.* [28] agree to within 10%. Both agree with data in a wide variety of cases. In particular, Shen *et al.*'s parametrization reproduces P and ^{16}O reactions in Si, and Tarasov *et al.*'s reproduces ^{32,34,36}S ions in C and Au. Shen's parametrization predicts that 0.3% of the incoming ions react in D_1, 0.4% in the Al foil, 0.6% in D_2, and 0.2% in D_3. Altogether, we therefore expect that a total of ≈1.5% of incoming ^{32}Ar ions should react.

However, the *good* ion cuts veto a significant fraction of those ions that would otherwise have been misidentified. For example, some of the fragmentation products would deposit energy in D_4. Predicting the exact fraction that is vetoed, however, requires a reliable model of the partial cross sections for all of the allowed channels. Unfortunately, neither parametrization predicts these partial cross sections. Models that *do* predict the partial cross sections include EPAX Version 2 [29], Silberberg and Tsao [30], and HZEFRG1 [31]. We found very poor agreement between these models, even under conditions where all three are expected to be valid.

The most difficult fragmentation channel to reject is $^{32-x}\mathrm{Ar} + x\,n$. Fortunately, all these models predict that a negligible fraction goes into this channel, as expected for fragmenting a proton-rich nucleus. Supporting evidence comes from a calculation [32] of the single neutron knock-out reaction cross section of ≈12 mb, which is ≈1% of the total calculated reaction cross section of ≈1500 mb. This negligible contribution is below systematic uncertainties, so we neglect neutron channels in the following analysis.

We have included reactions in our simulation using Shen *et al.*'s parametrization of the total reaction cross section. For the partial cross sections, one common aspect of all of the models considered is that the strongest channels are the ones with larger mass asymmetries, i.e., a heavy fragment close to the original ^{32}Ar mass and a light partner. We have considered a number of different reaction channels:

$$^{32}\mathrm{Ar} + {}^{A_t}Z_t \longrightarrow {}^{A_t}Z_t + \begin{cases} {}^{31}\mathrm{Cl} + p \\ {}^{28}\mathrm{S} + \alpha \\ {}^{25}\mathrm{Si} + {}^{7}\mathrm{Be} \end{cases} \qquad \text{(A1)}$$

Here $^{A_t}Z_t = (^{28}\mathrm{Si}, {}^{27}\mathrm{Al})$ is the target material (in the detectors and foil, respectively) where the reaction occurs. Our simple model assumes the target nuclei are not modified in the reaction and so are treated as spectators to the reaction. However, these nuclei do recoil, taking energy from the daughter fragments.

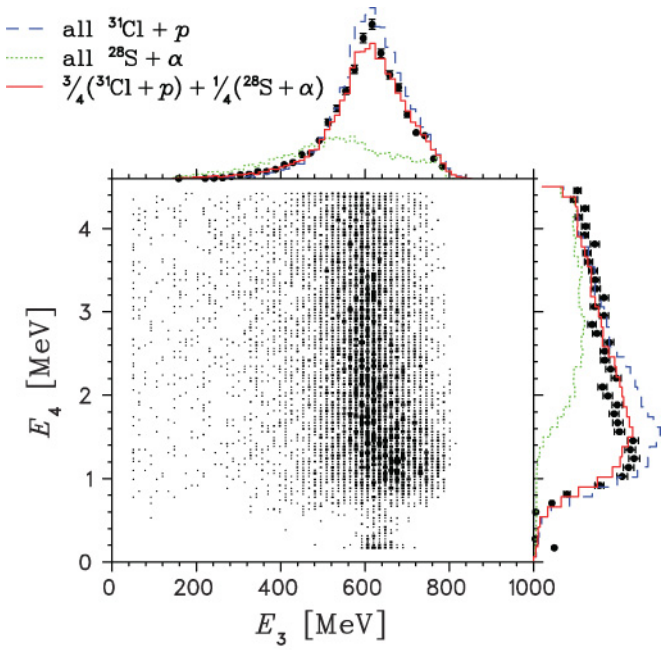

FIG. 17. (Color online) E_4 versus E_3 spectrum of events (roughly calibrated) in Region 3.1 of Fig. 3. In the projections, the data (points) are compared to our Monte Carlo simulation (histogram). Note that the Monte Carlo projections have *not* been rescaled to fit the data; the normalization is determined from the total number of ^{32}Ar.

This simple model predicts that two of our particle identification conditions can be used to veto events that correspond to reacted ions. According to LISE calculations and the results of subsection A2, we should not see *any* ^{32}Ar ions implanted in D_4. However, the E_3 vs. E_4 scatter plot gated by events in Region 3.1, Fig. 17, shows that some of these events result in a significant amount of energy deposited in D_4. Our simulations show that these events correspond to ions that reacted before coming to rest and that the resulting light fragment—with up to tens of MeV per nucleon—has enough energy to penetrate D_3 and deposit >800 keV in D_4. Our first condition, therefore, is to veto events for which $E_4 > 800$ keV. To efficiently tag reacted events in this way, we would need 4π coverage around the detectors. We estimate that our apparatus gave a vetoing efficiency of (50–75)%, depending on which reaction channel is considered (the least efficient being the p and α channels). Of the 1.5% incoming ions that react, simulations predict that an $E_4 < 800$ keV cut should reduce the contamination to (0.4–0.8)%: a reduction of $(1.1 - 0.7)\%$. In fact, we observed that this cut eliminated 0.8% of the *good* ion candidates.

Region 5.1 of the E_2 vs. E_3 spectrum is the other particle identification condition we use to preferentially veto reacted ion events. When applying this extra condition to the data, we observe that the change in the branch with and without the $E_4 < 800$ keV condition goes to 0.15%. This is also roughly consistent with the Monte Carlo prediction of (0.2–0.3)%. Figure 18 shows a comparison similar to the one shown in Fig. 17, but with the additional condition that ions were in Region 5.1.

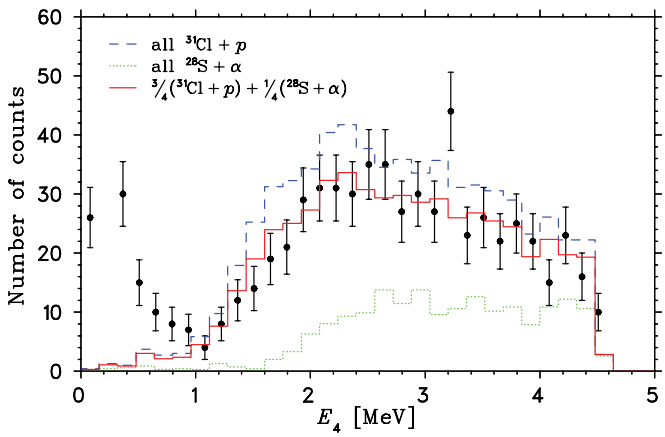

FIG. 18. (Color online) E_4 spectrum (roughly calibrated) of events in Region 3.1. This is similar to Fig. 17 but with the extra condition on Region 5.1.

We estimated the fragmentation correction and its uncertainty by taking two extreme cases. As one extreme, we assume no reactions survive our cuts. As the other extreme, we assume all of the reactions proceed through the $^{31}\mathrm{Cl} + p$ channel because this is the one with the poorest vetoing efficiency. The contamination level that remains after all our cuts are made is the maximum value from scheme 4 of Table VI, i.e., 0.2%. We assign a 100% uncertainty that yields

$$N_{\mathrm{Ar}} = N_{\mathrm{Ar}}^{\mathrm{uncorr}} \times 0.998(2). \tag{A2}$$

E. Delayed proton detection efficiency

Ions that are implanted too close to the surface of the detector (the range of a 3.35-MeV proton in Si is ≈0.1 mm) may emit protons outside the active area of the detector, leaving too little energy to be clearly identified, thereby making it appear as though the proton branch is smaller than it is. We will first consider implantation close to the rim and then near the upstream and downstream surfaces.

TABLE VI. Effect of particle identification conditions on the superallowed proton branch [see Eq. (7)]. The results are normalized to $b_{\mathrm{SA}}^{\beta p} = 20.83\%$, the result using our nominal analysis scheme without any corrections for contamination from reacted ions. For comparison, we also list the Monte Carlo calculated prediction of the fraction of events misidentified as ^{32}Ar ions.

Scheme	Conditions			$\Delta b_{\mathrm{SA}}^{\beta p}$	Monte Carlo contamination level
	Reg. 3.1	Reg. 5.1	$E_4 <$ 0.8 MeV		
1.	x			−1.00%	1.5%
2.	x		x	−0.19%	(0.4–0.8)%
3.	x	x		−0.05%	(0.3–0.5)%
4.	x	x	x	+0.10%	(0.1–0.2)%

TABLE VII. Ratios of heavy-ion count rates in detectors D_1, D_2, and D_3. We used these measurements to put an upper limit on the fraction of ^{32}Ar ions that could have been implanted in a region where protons would not be detected with high efficiency.

	R_2/R_1	R_3/R_1
^{32}Ar without collimator	0.9370	0.9065
^{28}Al without collimator	0.9504	0.9107
^{28}Al with collimator	0.9194	0.9170

1. *Implantation near the edges of* D_3

In the extreme case where the distribution of ^{32}Ar beam over the surface of D_3 was uniform, the fraction of ions implanted in the region where the proton detection efficiency is less than unity would be $\delta r/r \approx 8 \times 10^{-3}$. However, the distribution of the ^{32}Ar beam was far from uniform. This was verified during the latter part of the experiment when we produced a ^{28}Al beam for calibration purposes and introduced a collimator upstream of D_2 that blocked 40% of its active area. The fractional changes in the counting rates of incoming ions in this setup (listed in Table VII) showed that the implantation profile was concentrated near the center of the detector. Simulations based on a combination of LISE and GEANT [17] were used to estimate the characteristics of the incoming ion beam. The energy of the ^{28}Al and the ^{32}Ar ion beams were taken from LISE, and GEANT was used to track the ions through the system. We varied the beam width and divergence until the results listed in Table VII were reproduced. The simulations imply that 7×10^{-4} of the implanted ions landed near the rim. Further simulations that also tracked the emitted protons from these events suggest that only ≈1/7 of them would have had their signals degraded enough to fall outside the peak window. We conclude that the effect is negligible.

We also studied the effect of ^{32}Ar ions that landed just outside the active region of the detector. These ions would not be labeled as *good* ions, yet they could have emitted protons into the active area that would be counted as a valid decay event. Our simulations predicted that a negligible fraction of such events leave enough energy to be counted as decay events.

2. *Implantation near the up- and downstream surfaces of* D_3

We estimated the uncertainty from possible implantations near the downstream and upstream surfaces of the detectors using the D_3 decay energy spectra in coincidence with D_2 or D_4 shown in Fig. 19. These spectra provide information both about the mean of the implantation profile and its width because the peak energies are the sums of the energy of the β-delayed protons and the energy left in D_3 by the preceding βs. Because D_2 and D_4 subtended different solid angles at D_3 the spectrum in coincidence with D_2 has only ≈65% of the events as compared to that in coincidence with D_4 and the widths of the proton groups are different for the two spectra. However, our simulations show that the energies corresponding to half of the peak intensity on the lower energy side should coincide if the ^{32}Ar ions had been implanted exactly at the center of D_3. This is expected because this point would correspond to the proton energy plus the energy left by βs traveling through

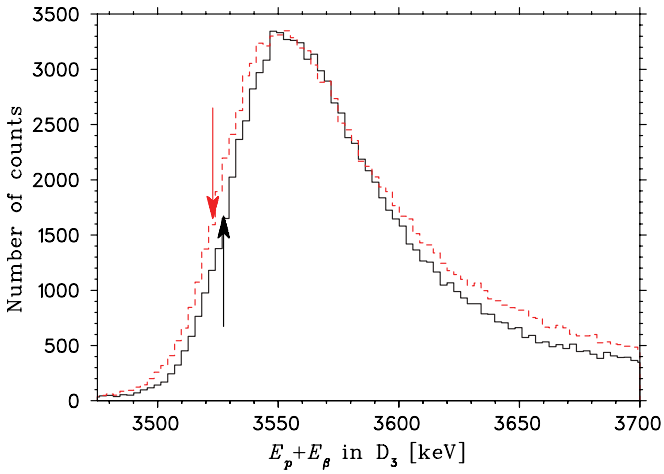

FIG. 19. (Color online) Superallowed proton peak in D_3 coincident with D_2 (solid line) or D_4 (dashed line). The difference in widths is due to the differing solid angles covered by D_4 and D_2. The curve for the coincidences with D_4 has been multiplied by 0.65 to show more clearly the energy shift. The arrows should coincide if the ^{32}Ar's were implanted exactly in the center of D_3.

the minimum amount of detector, i.e., along the beam axis, and so is independent of the solid angle. The observed energy difference of $\Delta E = 4.5(3)$ keV between the two spectra at the half peak-intensity points (indicated by the arrows) implies that the mean implantation depth is $9(1)\,\mu$m from the center of D_3 in the direction of D_4. The widths of the peaks in Fig. 19 are sensitive to the width of the implantation distribution. The distribution of ions within D_3 can be estimated from a LISE calculation using the fragment separator settings from Sec. II; Monte Carlo simulations using this nominal distribution (shown in Fig. 19) agree well with the data, whereas profiles with double that width—which would be wide enough that some protons could escape before stopping—are strongly excluded. We conclude that the probability for a 3.5-MeV proton escaping D_3 without depositing all of its energy is negligible ($\approx 8 \times 10^{-5}$).

F. γ branching ratio

Gamma feeding of the ^{32}Cl $T = 2$ state is highly unlikely. Given that the $T = 2$ state lies at $E_x \approx 5$ MeV, and the β-end-point energy is at $E_x \approx 10$ MeV, the phase space for β decays to levels above the $T = 2$ state decreases very rapidly. Also, the first $T = 2$ state will have a vastly larger β-decay matrix element than any other daughter state. Finally, the only states above the IAS that can be fed by allowed β decay are $T = 1$ levels, whose proton decays, unlike those of the IAS, are not inhibited by isospin selection rules; as a result their γ decays are unlikely to compete with proton decay.

We estimated the uncertainty in the shape of the predicted efficiency curve by performing simulations with significantly different geometries for the Ge crystals. In particular, we increased dead layer thicknesses by $20\,\mu$m and 2 mm for the outer and inner surfaces, respectively, and increased the lengths of the crystals by 2 mm. The change in the shape of the efficiency curve between the highest statistics peak from ^{32}Ar (3.9 MeV) and the nearest high-statistics peak from ^{32}Cl (4.8 MeV) was negligible.

The absolute γ-ray efficiencies of the Ge detectors depend on the solid angle subtended by the detectors. Our method of efficiency calibration relative to the ^{32}Cl decay lines is self-correcting, so the effects of variations in solid angle end up being negligible. This is not true for summing corrections because ^{32}Cl and ^{32}Ar have different multiplicities; we investigated the sensitivity of the summing correction with respect to the solid angle by comparing the calculations to one with an additional 5 mm offset in the position of all the Ge detectors. This uncertainty in the position of the detectors led to a summing correction uncertainty of $\pm 0.02\%$ in $b_{\mathrm{SA}}^{\beta\gamma}$.

The uncertainty in the efficiency normalizations that result from the fits shown in Fig. 13 arises from three sources:

(i) the statistical uncertainty due to the number of counts in the peaks corresponding to γ-decays from the isobaric analog state in ^{32}Cl following the superallowed β decay of ^{32}Ar. Only 1.92% of ^{32}Ar β decays results in one of these γs, so the statistics is relatively small and contributes $\Delta b_{\mathrm{SA}}^{\beta\gamma} = 0.08\%$.

(ii) the statistical uncertainty from the number of counts in the γ-calibration peaks. As the branching ratio is much higher in this case (only $\sim$1% of ^{32}Cl β decays are directly to the ground state), this uncertainty ends up being only $\pm 0.03\%$ in $b_{\mathrm{SA}}^{\beta\gamma}$.

(iii) the precision of the measured branching ratios of the calibration peaks [20] contributes another $\pm 0.03\%$ to the uncertainty in $b_{\mathrm{SA}}^{\beta\gamma}$.

The total uncertainty in $b_{\mathrm{SA}}^{\beta\gamma}$ from the γ branching ratio, dominated by the small statistics in the ^{32}Ar γ peaks, is $\Delta b_{\mathrm{SA}}^{\beta\gamma} = \pm 0.09\%$.

[1] J. C. Hardy and I. S. Towner, Phys. Rev. Lett. **94**, 092502 (2005).
[2] I. S. Towner and J. C. Hardy, Phys. Rev. C **77**, 025501 (2008). We quote the $\mathcal{F}t$ value that TH use when extracting V_{ud}, which includes a 0.85(85) s correction to account for variations between two different ways of computing δ_C.
[3] Calculation by B. A. Brown using the configuration-mixing plus mean-field method of Ref. [4] but with the SKx Skyrme interaction of Ref. [5].
[4] W. E. Ormand and B. A. Brown, Phys. Rev. Lett. **62**, 866 (1989).
[5] B. A. Brown, Phys. Rev. C **58**, 220 (1998).
[6] W. E. Ormand and B. A. Brown, Phys. Rev. C **52**, 2455 (1995).
[7] I. S. Towner, J. C. Hardy, and M. Harvey, Nucl. Phys. **A284**, 269 (1977).
[8] I. S. Towner and J. C. Hardy, Phys. Rev. C **66**, 035501 (2002).
[9] E. Hagberg, V. T. Koslowsky, J. C. Hardy, I. S. Towner, J. G. Hykawy, G. Savard, and T. Shinozuka, Phys. Rev. Lett. **73**, 396 (1994).
[10] A. García *et al.* (in preparation).
[11] J. Yorkston *et al.*, Nucl. Instrum. Methods A **262**, 353 (1987).

[12] See, for example, G. Duchêne *et al*., Nucl. Instrum. Methods A **432**, 90 (1999).
[13] L. code, D. Bazin, O. Tarasov, M. Lewitowicz, and O. Sorlin, Nucl. Instrum. Methods A **482**, 307 (2002).
[14] E. G. Adelberger, C. Ortiz, A. García, H. E. Swanson, M. Beck, O. Tengblad, M. J. G. Borge, I. Martel, H. Bichsel, and the ISOLDE Collaboration, Phys. Rev. Lett. **83**, 1299 (1999).
[15] T. Bjornstad *et al*., Nucl. Phys. **A443**, 283 (1985).
[16] F. C. Barker, Aust. J. Phys. **22**, 293 (1969).
[17] CERN *GEANT Detector Description and Simulation Tool*, Oct. 1994 version, 1993. We use GEANT instead of PENELOPE only when we are required to track protons or heavy ions that are not available in PENELOPE.
[18] J. Sempau *et al*., Nucl. Instrum. Methods B **132**, 377 (1997). Distributed by OECD Nuclear Energy Agency Data Bank.
[19] J. W. Martin, *et al*., Phys. Rev. C **73**, 015501 (2006).
[20] C. Dètraz, *et al*., Nucl. Phys. **A203**, 414 (1973).
[21] K. Blaum *et al*., Phys. Rev. Lett. **91**, 260801 (2003).
[22] I. S. Towner (private communication).
[23] S. Triambak *et al*., Phys. Rev. C **73**, 054313 (2006).
[24] P. M. Endt, Nucl. Phys. **A521**, 1 (1990).
[25] B. A. Brown and B. H. Wildenthal, Annu. Rev. Nucl. Part. Sci. **38**, 29 (1988).
[26] G. Audi and A. H. Wapstra, Nucl. Phys. **A595**, 409 (1995). We quote the value given in the compilation.
[27] W.-Q. Shen, *et al*., Nucl. Phys. **A491**, 130 (1989).
[28] O. B. Tarasov, *et al*., Nucl. Phys. **A629**, 605 (1998).
[29] K. Sümmerer and B. Blank, Phys. Rev. C **61**, 034607 (2000).
[30] R. Silberberg and C. H. Tsao, Astrophys. J. Suppl. **25**, 335S; L. Sihver, C. H. Tsao, R. Silberberg, T. Kanai, and A. F. Barghouty, Phys. Rev. C **47**, 1225 (1993).
[31] L. W. Townsend *et al*., NASA Technical Paper NASA-TP-3310, May 1993.
[32] We thank Jeff Tostevin for contributing to this calculation (private communication).